Journal Title
XX(X):1–16

DOI: 10.1177/ToBeAssigned
www.sagepub.com/
SAGE

A comparative study of the combustion of methane in a spark-ignited engine using CO_2-diluted oxidizer mixtures

Daese Mauro[1], Gabriele D'Antuono[3], Davide Lanni[3], Enzo Galloni[3], Francesco Contino[2] and Joshua Lacey[1]

Abstract

To investigate a potential method to eliminate NOx and facilitate carbon capture in reciprocating engines for stationary power generation, an experimental and numerical study is conducted to understand the effect of CO_2 dilution on the performance of oxy-CH_4 combustion in an air-cooled SI engine. Experiments are conducted at constant fuel mean effective pressure (fMEP) and at maximum brake torque (MBT) spark timing while the N_2 in the oxidizer is gradually replaced by CO_2 and the effect on engine performance is quantified. The increased CO_2 dilution results in a decrease in the ratio of specific heats (γ) and flame speed. Due to the significant thermal quenching effect of CO_2, there is an overall decrease in cylinder pressure and temperature leading to a total decrease of indicated efficiency, even when operating in a significantly oxygen-enriched environment. The interplay between turbulent flame propagation and the composition of generalized oxidizer mixtures consisting of O_2, N_2 and CO_2 is further explored using predictive modelling and compared with premixed, turbulent combustion theory. This analysis ultimately demonstrates that the dilution limit of the oxy-CH_4 combustion event is captured by the previously developed premixed combustion theory when compared against an experimental measurement of combustion instability, and that this instability is largely driven by the change of thermal mixture properties due to the introduction of large quantities of CO_2.

Keywords

CO_2 dilution, oxy-fuel combustion, laminar flame speed, premixed turbulent combustion theory, predictive modelling

Introduction

The energy transition towards renewable sources of generation is essential to achieve net-zero emission of greenhouse gases by 2050 [1]. However, the intermittency of generation from sources such as solar and wind guarantees the continuing need for highly dispatchable power during times of peak demand. One option to address this requirement is through the use of reciprocating engine power plants; in the EU, 30 GW of such engines contribute to power generation, representing approximately 15% of the current installed wind capacity across the member states. Due to their high dispatchability and ramping capabilities, the internal combustion (IC) engine power plant is an ideal technology for peaking and grid stability [2]. However, these engine power plants that currently operate on fossil fuels emit CO_2 and pollutants such as oxides of nitrogen, or NOx [3], which itself has substantial greenhouse gas warming potential (GWP). An advanced combustion technique known as oxy-fuel combustion is a potential solution to mitigate these undesirable species emitted from IC engines. Oxy-fuel combustion is a process in which a fuel is combusted in the presence of oxygen rather than air, eliminating N_2 in the intake mixture and therefore avoiding NOx formation. Additionally, such engines can directly valorize streams of O_2 produced after water electrolysis for green hydrogen production. While CO_2 is still emitted if combusting natural gas, the high concentration of CO_2 in the exhaust compared with conventional combustion greatly reduces the cost and complexity of carbon-capture [4, 5]. If using carbon-neutral, e-methane, a method for long-term seasonal storage in highly renewable grids [6, 7, 8], the capture of CO_2 emissions from an oxy-fuel engine could even result in net-negative CO_2 operation. Despite these compelling possibilities, oxidizing CH_4 stoichiometrically with no diluent would result in peak combustion temperatures in the range of 2500°C to 3000°C [9], which would likely result in mechanical damage to the engine[10]. Researchers have investigated various diluent options to mitigate this issue, such as H_2O, Ar and CO_2 [11, 12, 13, 14, 15, 16, 17]. Among these choices, CO_2 is perhaps the most economically feasible for oxy-methane combustion, as it can be recycled from the combustion products by condensing out water in the exhaust. Despite this, its use in reciprocating engines also introduces challenges in terms of its high molar specific heat capacity (C_p) and density compared to nitrogen, leading to reduced flame speeds, increased combustion duration and longer time for heat losses [11, 18, 19]. Oxy-fuel combustion with

[1]Department of Mechanical Engineering, KU Leuven, Belgium
[2]Institute of Mechanics, Materials and Civil Engineering (iMMC), UCLouvain, Belgium
[3]Department of Civil and Mechanical Engineering, University of Cassino and Southern Lazio, Italy

Corresponding author:
Daese Mauro, Department of Mechanical Engineering, KU Leuven, Leuven, Celestijnenlaan 300, 3001, Belgium.
Email: mauro.daese@kuleuven.be

CO_2 dilution has been previously considered in combustors and gas turbines as a method to obtain cleaner combustion products in power generation [20]. However, the lower thermal efficiency and inferior emissions of gas turbines in comparison to IC engines was noted in this previous work [21, 22], and the use of gas turbines in low and medium-range power plants was often more expensive when compared to IC engines [23]. Moreover, gas turbines are less suitable for fast-ramping, peaking demands in comparison to IC engines [2], and according to a recent investigation by Seo et al. [24], oxy-fuel power plants are economically feasible. While they incur a higher initial cost and experience an additional energy loss compared to air-fuel power plants, the study supports their overall economic viability. As increasing renewable generation on the grid will shift the need towards smaller power plants for peaking generation, there is strong motivation to explore cleaner methods of combustion in IC engines, such as oxy-fuel combustion. To this end, there has been limited experimental investigation of oxy-fuel combustion in reciprocating engines, with the earliest such studies conducted for compression ignition (CI) engines operating with diesel fuel. The concept of oxy-fuel combustion was proposed in 1982 by Abraham et al. [25] and in the following year, the first oxy-fuel combustion engine was tested by Shaw and Omar [26]. These earlier engines were termed closed-cycle diesel engines (CCDE) and were used in submersible, unmanned marine applications. Zheng et al. [27] experimented with a non-air-breathing underwater diesel engine that used a CO_2 scrubber for recirculating the exhaust gasses, and the use of such CCDEs was intensively tested further as underwater autonomous vehicle drivers for military applications by Hawley et al. [28, 29, 30], though a decrease in thermal efficiency was observed compared to conventional compression ignition (CI) with diesel fuel. Improvement was observed when ethanol or gasoline were port-fuel injected into a CCDE as shown by Wu et al. [31], with ethanol more effective in the reduction of smoke and post-combustion CO_2 than gasoline. Though there were promising results for underwater applications at that time, it was noted that the practical implementation of such an engine for a transport was not cost-efficient. Further, undesirable emissions of soot and particulates that are characteristic of non-premixed CI combustion were still present in the oxy-fuel CCDEs. Therefore, there is strong motivation to investigate oxy-fuel combustion in premixed (such as spark-ignition or SI) reciprocating engines, which avoid such emissions, for stationary power generation applications. To date, there has been limited study of premixed oxy-fuel combustion in reciprocating engines, and the work that does exist is primarily numerical. SI oxy-propane combustion with O_2 enrichment was investigated through numerical simulation by Wu et al. using water injection as a means to control peak combustion temperatures [32]. Methods to mitigate the combustion-inhibiting effects of water injection were studied in simulation through the use of exhaust gas recirculation (EGR) [33, 34]. Experimentally, stoichiometric SI oxy-CH_4 experiments and flame speed predictions were performed by Van Blarigan et al. [11, 18] with CO_2 and EGR as the oxidizer components using an O_2 concentration above 21%. Though these experiments were performed using hardware that is less relevant to modern reciprocating engines (a CFR engine), this earlier work was instrumental in highlighting the aforementioned challenges of CO_2-diluted oxy-methane combustion. Serrano et al. [10] investigated the combustion process and engine outputs during oxy-fuel operation in a SI ICE. Taking the thermo-mechanical constraints into account, the findings suggested that using EGR or other inert species is more feasible than using pure oxygen for the oxidizer. Despite these previous efforts, a comprehensive understanding of oxy-methane combustion, and in particular its instability limits in SI engines, is not yet well established. This knowledge will be essential before such technology can be realized industrially. Therefore, the current work seeks to provide a detailed characterization of CO_2-diluted oxy-methane combustion in SI engine hardware. In doing so, this study will develop a new, general laminar flame speed correlation for methane flames in oxidizer streams ranging from air to mixtures of O_2 and CO_2. Further, the work will investigate a predictive methodology of the instability limit for a generalized oxidizer stream, a necessity for the successful development of oxy-fuel engines, using premixed turbulent combustion theory [35, 36]. The fidelity of this prediction will be assessed by comparison with a quantification of combustion instability from an experimental measurement of in-cylinder pressure. In doing so, the current work will determine the wider applicability of such theory to describe oxy-fuel combustion through theoretical prediction. To accomplish this, the study relies on coupled experimental measurements and reduced-order numerical simulation.

Experimental setup

The experiments are performed on a single-cylinder SI engine specifically developed for oxy-fuel combustion, which is modified from a single-cylinder Yanmar diesel engine. Table 1 provides the specifications of the engine and Figure 1 shows a visualization of the test bench. Modifications were made to the cylinder head to introduce a spark plug, a thermocouple and an in-cylinder pressure sensor. Additionally, the compression ratio was reduced from the factory configuration to 9.8 and the valve timing was modified to remove overlap. These modifications were performed to avoid any potential autoignition with oxygen-enriched environments and to the recirculation of residual gasses. The ignition timing (IT) is controlled and regulated using a MoTeC M84 ECU. The in-cylinder pressure is measured by a piezoelectric AVL GH15D pressure sensor which is then amplified by an AVL FlexIFEM 2P2E. The mass flow of fuel and oxidizer into the engine cylinder is controlled by Brooks mass flow controllers (MFC) of the SLA-585x series. Fuel/oxidizer mixture and exhaust gas pressures are measured by two KISTLER 4260

Table 1. Characteristics of SI engine used for experimentation.

Engine type	Air-cooled, Single-cylinder
Make	Yanmar L100V
Displacement [L]	0.4357
CR	9.8
Bore (b) [mm] · Stroke (L) [mm]	86 · 75
Connecting rod length (l) [mm]	120.5
Crack radius (r_c) [mm]	37.5
IVO - IVC [CAD]	0 ATDC - 233 ATDC
EVO - EVC [CAD]	-233 ATDC - 0 ATDC

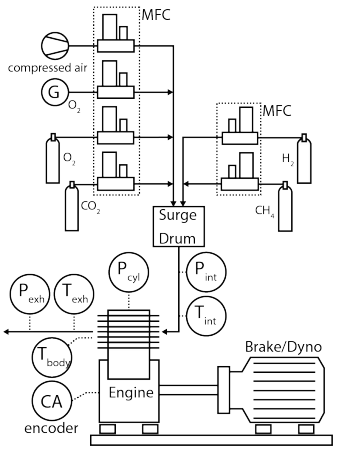

Figure 1. Experimental setup schematic

transducers. The intake temperature, exhaust temperature and the cylinder wall temperature are measured using three K-type thermocouples. An electric motor is coupled to the engine crankshaft to maintain constant speed operation at 1500 RPM (charachteristic of stationary power generator sets producing electricity at 50 Hz) and a HBM T40B torque sensor with a flange connection is mounted on the connecting shaft between the motor and engine. A Heidenhain ROD 426 rotary crank angle encoder with the ability to record 3600 samples per revolution is used to acquire the relative positions and provide the sample clock for the acquisition of in-cylinder pressure. The raw data is acquired by an NI cRio 9022 module. Based on the volume required by the engine, O_2 is provided by either a high pressure O_2 cylinder (low flow) or Noxerior OP-60 Ecoline pressure swing adsorption O_2 generator (high flow). The O_2 generator can produce O_2 at 95% purity. The sources of experimental uncertainty include those found in the MFC readings, the purity of supplied gasses, the crank angle encoder position, the in-cylinder pressure signal and intake and exhaust pressure sensors. Table 2 shows a summary of the uncertainties of various instruments used in experimentation. In Table 2, FS indicates the full-scale value and PV indicates the processed value. The methodology used for this uncertainty analysis is explained by Pochet et al [37]. In Table 3 the average uncertainties on the most significant quantities are reported.

Table 2. Summary of equipment uncertainty.

MFC (Brooks SLA585X)	Uncertainty
Accuracy	±0.7% PV
Repeatability	±0.2% FS
Temperature zero drift	±0.05% FS/K
Temperature span drift	±0.05% FS/K
Pressure drift	±0.429% PV/Bar
Gas cylinders (Air Liquide)	Purity
CH_4	99.5%
O_2	99.995%
CO_2	99.995%
Crank Angle Encoder	Uncertainty
Least Count	0.1 CAD
TDC positioning	±0.05 CAD
In-cylinder Pressure	Uncertainty
Signal amplifier	
Amplifier accuracy	±0.01% FS
Accuracy$_{G,amp}$	±0.5% (U95)
Intake & Exhaust Pressure	Uncertainty
Linearity + Repeatability	±0.2% FS
Age drift	±0.1% PV/year
Temperature drift	±1.5% PV

Table 3. Average uncertainties on the most significant quantities.

Parameter	U_{95}
γ	$\leq$ 0.05 %
p_cyl (CA10-CA90)	$\leq$ 0.5 Bar
V	$\leq$ 1.9 %
Q_{net}	$\leq$ 1 %
CA2, CA10, CA50, CA90	$\leq$ 0.2 CAD
S_L	$\leq$ 0.2 %
K and Da	$\leq$ 0.4 %
IMEP, η_i	$\leq$ 0.24 %
Species	$\leq$ 1.2 %

Methodology

The following sections first describe the operating conditions explored in this study and define the experimental operating parameters. The reduced-order model in GT-Power that is utilized for heat release analysis and predictive modeling of the combustion event is then discussed. In particular, the manner in which necessary parameters are determined from the numerical model in order to employ relevant premixed turbulent combustion theory is highlighted.

Experimental operating conditions

The non-dimensional fuel/oxidizer mixture strength used in the experiments is defined by the ratio λ'. In principle, this ratio is similar to the equivalence ratio for the conventional combustion process, however, only O_2 is considered and a different notation is used because the oxidizer is, in general, a mixture of gases other than air.

$$\lambda' = \frac{1}{\phi'} = \frac{\frac{\dot{m}_{O_2}}{\dot{m}_{CH_4}}}{\left\{\frac{\dot{m}_{O_2}}{\dot{m}_{CH_4}}\right\}_{stoichiometric}} \tag{1}$$

In Equation 1, $\dot{m}_{O_2}$ represents the flow of O_2 and $\dot{m}_{CH_4}$ represents the flow of CH_4 into the engine cylinder in kg/s. Table 4 shows five operating conditions which are selected from 21 in total to represent the full range of tested engine operation. V_{CO_2}, V_{N_2} and V_{O_2} are the volume percentages of CO_2, N_2 and O_2 respectively. The values are shown as a percentage of the oxidizer mixture or the complete entrained mixture containing both fuel and oxidizer. During the experiments, the injected fuel energy content is maintained as constant and is characterized by the so-called fuel mean effective pressure or fMEP. This quantity, in units of pressure, is the amount of fuel energy introduced into the cylinder normalized by the displacement volume and is given by Equation 2 [38].

$$\text{fMEP} = \frac{m_{CH_4} \cdot Q_{lhv}}{V_s} \tag{2}$$

In Equation 2, Q_{lhv} is the lower heating value of CH_4 in kJ/kg and V_s is the displacement volume in m^3. Because the injected fuel energy remains constant as the oxidizer mixture is changed, increasing oxygen enrichment implies that λ' is likewise increased. While other methods of operation will likely be explored in future work, the goal here was to not only build a robust set of oxy-methane data, but also to probe the limits of instability for both partial (some nitrogen still present) and full (all nitrogen replacement by oxygen and CO_2) CO_2-diluted oxy-fuel modes. As the engine is air-cooled, the thermal condition of the engine was closely monitored during the experimental campaign and also

Table 4. Operating conditions for experimentation.

Sl. No.	V_{N_2} (vol.% oxi.)	V_{O_2} (vol.% oxi.)	V_{O_2} (vol.%)
|⟷|	79 - 0	21 - 36	19 - 32.6
1	79	21	19
2	56.5	24.6	22.3
3	35.7	28.2	25.5
4	16.9	31.7	28.7
5	0	36	32.6

V_{CO_2} (vol.% oxi.)	V_{CO_2} (vol.%)	λ'	IT (CAD BTDC)
0 - 64	0 - 58	1 - 1.70	21 - 38
0	0	1	21
18.9	17.1	1.17	25 - 27
36.1	32.7	1.35	29 - 31
e 51.4	46.6	1.53	32 - 34
64	58	1.70	36 - 38

limited the capability to operate with oxygen-enrichment at mixtures approaching stoichiometry, hence the focus on the experimental conditions as previously detailed. The upper temperature limits used to define thermal cut-off point was 200°C for the block and 110°C for the oil. At these limits, the heat losses of the engine are deemed significant enough that further investigations become increasingly impractical. When performing parametric variations, the lower stability limit for combustion is exceeded if the coefficient of variance of IMEP ($\mathrm{CoV_{IMEP}}$) exceeds a value of 5% (often used as a benchmark in experiments, e.g. Heywood [38]) and is calculated with Equation 3.

$$CoV_{\mathrm{IMEP}} = \frac{100}{\overline{\mathrm{IMEP}}} \cdot \sqrt{\frac{1}{N} \cdot \sum_{i=1}^{N} (\mathrm{IMEP}_i - \overline{\mathrm{IMEP}})^2} \quad (3)$$

In Equation 3, IMEP_i represents the indicated mean effective pressure of the i^{th} cycle in $N = 100$ cycles that are considered for data acquisition and $\overline{\mathrm{IMEP}}$ is the average indicated mean effective pressure. To substantiate the statistical significance of the use of 100 cycles, the CoV_{IMEP} was investigated as a function of the number of cycles in the ensemble average. When considering more then 60 cycles, CoV_{IMEP} was asymptotic for the operating condition with the highest instability, and therefore 100 cycles was deemed sufficient for data analysis. The intake pressure of the engine is set to atmospheric pressure, to replicate a full load, naturally aspirated engine. This is done by operating the engine near maximum brake torque (MBT) with three different ITs. However, the correct IT is chosen at MBT when the peak pressure position is equal to 15 CAD ATDC per [38], and is confirmed by observing IMEP over spark timing sweeps using the experimental setup. The value of fMEP is always held constant with the values of λ' and V_{CO_2} changing accordingly.

For post-processing at each operating condition, a selection of pressure traces are made based on the median IMEP, median peak pressure and median peak pressure position. Based on an RMSE over the closed part of the cycle, the pressure trace closest to the mean pressure trace is chosen for post-processing, as it is considered to be representative of the operating condition and is an actual recorded, in-cylinder pressure profile. This selected pressure trace is post-processed by an in-house tool written in MATLAB and further analysed using a GT-Power model of the engine. The calculation of efficiency, the C_p of individual species in-cylinder and the rate of heat release, which are utilized in further discussions, are briefly described by the following equations in this section. The indicated efficiency (η_i) is a parameter used to access the total efficiency of the cycle, it is calculated by the ratio of IMEP and fMEP [38]:

$$\eta_i = \frac{\mathrm{IMEP}}{\mathrm{fMEP}} \quad (4)$$

The ideal efficiency, η_{ideal}, is calculated as in Heywood [38] and given by 7. Further, η_{dcv} is the degree of constant volume given by Equation 5 as suggested by Shudo and Nabetani [39].

$$\eta_{dcv} = \frac{1}{\eta_{ideal} \cdot Q_{HR}} \cdot \int_{IVC}^{EVO} 1 - \left(\frac{V_s + V_c}{V}\right)^{1-\gamma} \cdot \frac{dQ}{d\theta} \cdot d\theta \quad (5)$$

In the equation, Q_{HR} is the cumulative heat release rate in J. V_s and V_c are respectively the swept volume and clearance volume, V is the instantaneous volume in m^3 at a particular CAD. γ represents the ratio of specific heats and $dQ/d\theta$ is the net heat release rate in J/CAD given by Equation 8 as stated in Heywood [38]. The specific heat capacity at constant pressure of each species is individually determined with Equation 6, where the coefficients according to each species are taken from the NASA database [40]. The temperature, T is calculated via GT-Power and based on the ideal gas law.

$$\frac{C_p}{R} = \alpha_1 + \alpha_2 \cdot T + \alpha_3 \cdot T^2 + \alpha_4 \cdot T^3 + \alpha_5 \cdot T^4 \quad (6)$$

$$\eta_{ideal} = 1 - \frac{1}{CR^{\gamma_{mean}-1}} \quad (7)$$

$$\frac{dQ}{d\theta} = \frac{\gamma}{\gamma - 1} \cdot \frac{dV}{d\theta} + \frac{1}{\gamma - 1} \cdot V \cdot \frac{dp}{d\theta} + \frac{dQ_w}{d\theta} \quad (8)$$

In Equations 7 and 8, CR is the compression ratio and γ_{mean} is the mean of γ between IVC and EVO. p is the instantaneous pressure at a particular CAD. The wall heat losses $(dQ_w/d\theta)$ in J/CAD are given by Equation 9 and calculated using the Woschni's correlation [38].

$$\frac{dQ_w}{d\theta} = A \cdot h_c \cdot (T - T_w) \quad (9)$$

Here, A is the surface area of the combustion chambers in m^2, T and T_w are the mean temperature in the combustion chamber and the wall temperature, respectively. h_c is the convective heat transfer coefficient in $\mathrm{W/(m^2 \cdot K)}$ and is given by 10:

$$h_c = 3.26 \cdot b^{-0.2} \cdot p^{0.8} \cdot T^{-0.55} \cdot w^{0.8} \quad (10)$$

where b is the bore in m and w is a function of average position speed $(\overline{S_p})$ in m/s given by 11

$$\begin{cases} w = 2.28 \cdot \overline{S_p} & \theta < \mathrm{IT} \\ w = 2.28 \cdot \overline{S_p} + 3.24 \cdot 10^{-3} \frac{V_s \cdot T_{IVC}}{V_{IVC} \cdot p_{IVC}} \cdot (p - p_m) & \theta \geq \mathrm{IT} \end{cases} \quad (11)$$

Turbulent Flame Regime

The first step of the premixed combustion analysis is to characterize the combustion regime. Different regimes can be defined by several key non-dimensional parameters. The different regimes as defined in [38] are plotted as the Damköhler number (Da) as a function of the turbulent Reynolds number (Re_T).

$$Da = \frac{\tau_{flow}}{\tau_{chemical}} = \frac{\frac{L_T}{u_k^t}}{\frac{\delta_L}{S_L}} = \frac{L_T}{u_k^t} \cdot \frac{S_L}{\delta_L} \tag{12}$$

The Damköhler number is defined as the ratio between the flow timescale and the chemical timescale. In this equation L_T is the turbulent length scale, u_k^t is the turbulent intensity, S_L the laminar flame speed and δ_L is the laminar flame thickness which is defined as [35]:

$$\delta_L = \frac{\mu}{\rho \cdot S_L} \tag{13}$$

Where μ is the dynamic viscosity and ρ is the density. The turbulent Reynolds number is defined as:

$$Re_T = \frac{u_k^t \cdot L_T \cdot \rho}{\mu} = \frac{u_k^t}{S_L} \cdot \frac{L_T}{\delta_L} \tag{14}$$

Figure 14 shows the combustion regimes and indicates where SI engine combustion normally takes place in the highlighted region [38]. The goal of this work is to identify the effect that changing the oxidizer composition has on these non-dimensional parameters.

Development of the Bradley Diagram

Bradley et al. [35, 36] investigated the impact of turbulent strain on flame stretch and quenching at the lean instability limit, essentially quantifying the competing effect between turbulence promoting entrainment of unburned fuel/air mixture to the reaction zone and turbulence causing excessive flame stretch and eventual extinction of the flame. Abdel Gayed et al. [41, 42] developed a correlation for all available experimental data present at the time for turbulent burning velocities across a wide range of equivalence ratios for methane, propane, iso-octane, and hydrogen-air mixtures. This correlation uses dimensionless groups, including the Karlovitz stretch factor (K) [41, 42].

$$K = \frac{u_k^t}{l_T} \cdot \frac{\delta_L}{S_L} \tag{15}$$

In this equation, l_T is the Taylor microscale of turbulence, which is calculated in GT-Power as:

$$l_T = \frac{C_{TLSM} \cdot L_T}{\sqrt{Re_T}} \tag{16}$$

where C_{TLSM} is the Taylor length scale multiplier. Following from this equation, K can be alternatively calculate by substituting Equation 16 in Equation 15.

$$\begin{aligned} K &= \frac{1}{C_{TLSM}} \cdot \left(\frac{u_k^t}{S_L}\right)^2 \cdot \frac{1}{\sqrt{Re_T}} \\ &= \frac{1}{C_{TLSM}} \cdot \left(\frac{u_k^t}{S_L}\right)^{1.5} \cdot \left(\frac{\delta_L}{L_T}\right)^{0.5} \\ &= \frac{1}{C_{TLSM}} \cdot \frac{{u_k^t}^{1.5}}{S_L^2} \cdot \left(\frac{\mu}{\rho \cdot L_T}\right)^{0.5} \end{aligned} \tag{17}$$

Abdel Gayed et al. [43, 44] studied how the effects of strain interact with molecular thermal-diffusive processes, represented by the Lewis number (Le) of the original reactants. They concluded that higher Le values lead to a greater influence of flame straining. The Lewis number can be determined as the ratio of the thermal diffusivity (α) to the mass diffusivity:

$$Le = \frac{\alpha}{D_{ij}} = \frac{k_t}{\rho \cdot C_p \cdot D_{ij}} \tag{18}$$

where k_t and D_{ij} are the thermal conductivity and the mass diffusion coefficient respectively. The mass diffusivity is evaluated with Cantera using the mixture composition, temperature an pressure at the specific operating conditions. Abdel Gayed et al. [44] ultimately correlated flame quenching conditions with the product $K\,Le$. The 'Bradley diagram,' as illustrated in Figure 17, presents these quenching conditions in different regions of the diagram, alongside the empirically defined curves for $K \cdot Le$ and $Re_T \cdot Le^{-2}$. The diagram is plotted with the ratio of turbulent flame speed to laminar flame speed (S_T/S_L) on the y-axis and the ratio of turbulent intensity to laminar flame speed (u_k^t/S_L) on the x-axis. There are two ways to compute and plot the loci of a combustion event superimposed on the Bradley diagram, which offers insight into the potential for bulk quenching of the turbulent, premixed flame in a reciprocating engine. Firstly by directly evaluating Equation 14 and 17. The alternative possibility is by evaluating S_L, S_T and u_k^t. S_L is determined through a chemical kinetics simulation in CHEMKIN, which is described in the following section. S_T and u_k^t are obtained from the predictive turbulent combustion model of GT-Power. GT-Power's S_T value is an estimate for the apparent burning velocity or mean expansion speed of gas. From Heywood [38], S_T is calculated by:

$$S_T = S_{T_{GT-Power}} \cdot \frac{\left(\frac{T_u}{T_b} - 1\right) \cdot \text{MFB} + 1}{\frac{T_u}{T_b}} \tag{19}$$

Here, T_u and T_b are respectively the unburned and burned zone temperature. $K\,Le$ values for various operating conditions can be determined using Equation 20 for values between $K\,Le$ = 0.01 and 0.63 [36] and the extracted parameters from the predictive model (namely S_T and u_k^t). In later sections, these will be first compared against the directly calculated values from Equation 17 and then to an experimental measurement of combustion stability, i.e. CoV_{IMEP}, in order to assess the capability of turbulent premixed combustion theory to predict instability in oxy-methane combustion.

$$K\,Le = \left(\frac{S_T}{u_k^t \cdot 0.88}\right)^{\frac{-1}{0.33}} \tag{20}$$

Bradley et al. [35] further described similar regimes of turbulent flame propagation by analyzing schlieren cine films at various $K\,Le$ values and comparing the results with those previously proposed by Borghi [45]. By using a logarithmic plot of (u_k^t/S_L) and (L_T/δ_L), constant values of K and Re_T are represented by straight lines on the Borghi diagram, as shown in equations 17 and 14. Figure

15 outlines the boundaries of the combustion regimes with corresponding K values, as proposed by Borghi [45]. The diagram incorporates the more recent terminology introduced by Peters [46], with Borghi's original terms provided in brackets. In Figure 16, the diagram is shown with the analogous regimes suggested by Bradley et al. [35].

Prediction of laminar flame speed using CHEMKIN In order to run the predictive turbulent combustion model in GT-Power, it is essential to provide a correlation for S_L, as this is one of the essential parameters governing the combustion process. The GT-Power software has a built-in correlation for methane-air combustion, but it is not suitable for oxy-methane combustion. One functional form to describe laminar flame speed is given by

$$S_L = \left(B_m + B_{\phi'} \cdot (\phi' - \phi'_m)^2\right) \cdot \left(\frac{T_u}{T_0}\right)^{\alpha} \cdot \left(\frac{p}{p_0}\right)^{\beta} \quad (21)$$

where T_0 and p_0 are the reference temperature and pressure, and B_m , $B_{\phi'}$, ϕ'_m, α and β are constants depending on the operating condition [38]. The current work uses experimental measurements combined with CHEMKIN simulations to develop an expression for S_L that can be input into the GT-Power model of the engine. Several mechanisms were evaluated against experimental data found in literature to define the best fit for the operating conditions in this research. The RMSE is calculated from Equation 22 is used to determine a 'best fit' between simulated values and experimental measurements.

$$\text{NRMSE} = \sqrt{\frac{1}{n}\sum_{i=1}^{n}\left(\frac{S_{L_i} - \hat{S}_{L_i}}{S_{L_i}}\right)^2} \quad (22)$$

Here, S_{L_i} is the experimental value of the laminar flame speed and $\hat{S}_{L_i}$ is the numerical value of the laminar flame speed, both for operating condition "i". Based on the lowest RMSE between simulated and experimentally measured laminar flame speed across a range of equivalence ratio for both methane-air and oxy-methane flames, the Aramco 3.0 chemical kinetics mechanism appeared to be the best choice. This kinetic mechanism was selected to calculate S_L per Zhou et al. [47]. Figure 2 shows the comparison of the

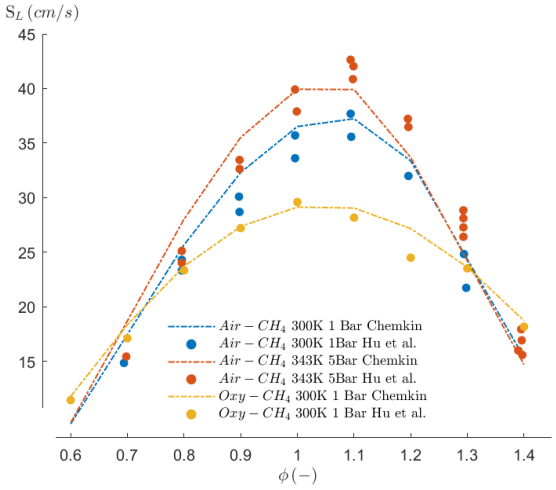

Figure 2. Validation of CHEMKIN simulation with experimental data

Table 5. Laminar flame speed correlation constants.

Sl. No.	B_m (cm/s)	$B_{\phi'}$ (cm/s)	ϕ'_m	α	β
1	36.77	-131.65	1.07	1.91	-0.35
2	30.17	-98.41	1.07	2.24	-0.48
3	28.54	-90.16	1.06	2.35	-0.52
4	28.55	-85.54	1.06	2.55	-0.58
5	31.50	-92.02	1.05	2.63	-0.58

Aramco 3.0 model with 3 sets of data that include the S_L values for air-CH_4 at 300 K and 1 bar, 443 K and 5 bar [48] and oxy-CH_4 at 300 K and 1 bar (35% O_2 & 65% CO_2) [49] at a range of λ'. The first part of the correlation (Equation 21) describes a ϕ'-sweep at reference conditions (i.e. T = 298K and P = 1 atm). This simulation is performed in CHEMKIN and a regression is made to define B_m, $B_{\phi'}$ and ϕ'_m. The second part of the correlation describes the impact of temperature and pressure changes. A set of different pressures and temperatures centered around the in-cylinder conditions of those operating conditions are simulated. A 2D regression was applied to define the values for α and β. In Table 5 the values of B_m, $B_{\phi'}$, ϕ'_m, α and β are presented. As shown in Table 5, ϕ'_m remains relatively constant, while both B_m and $B_{\phi'}$ exhibit a decreasing trend. A linear relationship has been observed between B_m, $B_{\phi'}$, and the concentrations of N_2 and CO_2. Additionally, following the observations of Heywood [38], a linear trend is also evident for α and β as a function of ϕ'_m.

GT-Power predictive combustion modelling A model of the single-cylinder engine and test bench layout was implemented in the GT-SUITE software framework. The experimental data was used to validate the reverse run simulations (i.e. calculate $\frac{dQ}{d\theta}$ from in-cylinder pressure) and these were in turn used to validate the predictive turbulent combustion model. The model was first calibrated with a motoring pressure trace. This provided a basis to verify the reverse run simulation using data under conventional SI CH_4-air conditions at 1500 RPM. Equation 23 shows the normalised root mean square error (NRMSE) of pressure for the comparison between simulated and measured in-cylinder pressure.

$$NRMSE = \sqrt{\frac{1}{N}\cdot\sum_{i=1}^{N}\left(\frac{p_{sim}(i) - p_{meas}(i)}{p_{meas}(i)}\right)^2} \quad (23)$$

where p_{meas} and p_{sim} are the in-cylinder pressure obtained from measurement and simulation over the crank angle, respectively, and N is total number of crank angle samples. Here, a threshold of NRMSE equal to 5% was chosen as the convergence criterion for the simulations, per that established in previous work [50]. In Table 6, the NRMSE values of the reverse run (RR) and predictive model (PR) are shown. The built-in optimization tool of GT-Power is used to calibrate turbulent flame speed to match $\frac{dQ}{d\theta}$ of the predictive model and reverse run simulations as close as possible. This is done by adjusting the Taylor Length Scale Multiplier (C_{TLSM}), Turbulent Flame Speed Multiplier (C_{TFSM}) and Flame Kernel Growth Multiplier (C_{KGM}). In Table 6 the values found for the five investigated operating conditions can be found.

Table 6. Calibration constants used in the predictive GT-power model.

Sl. No.	RR	PR	C_{TLSM}	C_{TFSM}	C_{KGM}
1	0.019	0.018	7.409	0.967	5.341
2	0.011	0.016	5.378	0.611	6.220
3	0.008	0.019	3.358	0.561	6.636
4	0.009	0.014	2.760	0.553	5.375
5	0.009	0.019	2.251	0.419	4.443

Assessing in-cylinder flow characteristics One of the input requirements for the predictive GT-Power model are the flow characteristics of the engine. This input is provided to a submodel that ultimately initializes the in-cylinder turbulence at IVC (the closed portion of the cycle). To obtain a reasonable approximation of flow through the engine, a RANS CFD model is employed. AVL Fire is used to develop a mesh and to perform a motored cycle based on experimental measurements. This approach has already been used in previous work for a CNG fueled engine as in [51]. Starting from the engine geometry, a mesh of approximately 1.5 million elements at BDC was implemented as shown in Figure 3. To perform the

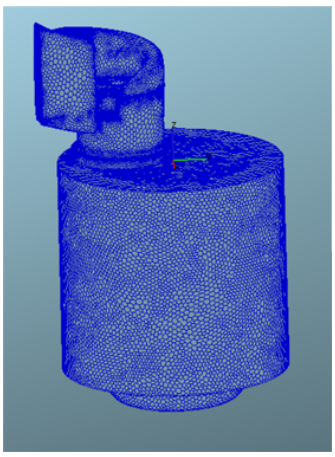

Figure 3. CFD mesh for flow simulations

simulation, a first-order (Euler) implicit differencing scheme was used for time discretization, while second-order schemes were used for the continuity and momentum equations. Finally, the turbulent effects were described by means of the standard k-ζ-f approach, per that established in previous work [52]. For the initial and boundary conditions, ambient conditions are considered and wall temperatures are set equal to 298 K, while the inlet pressure is equal to 0.96 bar. The results of the simulation are presented in Figure 4. The swirl number (S_n), tumble number (T_n) and normalized turbulent intensity by mean piston speed ($\frac{u_k^t}{u_p}$) are shown as a function of CAD. The turbulent length scale (L_T) normalized by the cylinder diameter is not presented in the figure because its values are several orders of magnitude smaller. The values at IVC are taken as input for the flow model in GT-Power, the value of turbulent length scale (L_T) normalized by the cylinder diameter is 0.003 at IVC. No experimental flow-field data are available for the engine, which introduces a degree of uncertainty since the model cannot be directly validated against measurements. Moreover, the 0D combustion model does not explicitly resolve spatial effects arising from the turbulent flow field. Consequently, this source of uncertainty is likely subsumed within the broader uncertainties associated with representing turbulence in an inherently 0D framework.

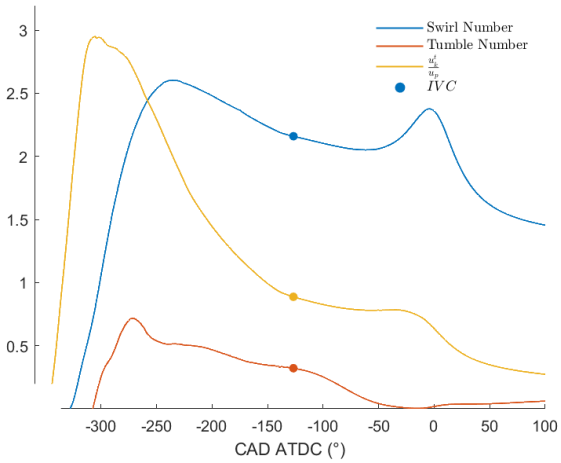

Figure 4. S_n, T_n and $\frac{u_k^t}{u_p}$ for motoring conditions

Experimental results

Effect of changing oxidizer mixture on combustion pressure, temperature and γ

Figure 5 and 6 shows the in-cylinder pressure and temperature plots with respect to CAD ATDC between IVC and EVO with different oxidizer compositions. It is shown that as CO_2 replaces N_2 in the oxidizer mixture and λ' increases, there is a decrease in temperature and pressure in the compression stroke, which is largely due to a higher value of C_p and a lower value of γ for CO_2. CO_2 has a pronounced thermal effect, acting as a more effective heat sink in the combustion chamber than nitrogen. The variation in γ can be seen in Figure 7, where it is clear that there is

Table 7. S_L, CoV_{IMEP} and η_i for every operating condition.

Sl. No.	$S_L\ (cm/s)$	$CoV_{IMEP}\ (\%)$	$\eta_i\ (\%)$	$T_{exh}\ (K)$
1	84.3	0.46 - 0.57	34.1 - 34.8	883
2	54.0	0.64 - 1.16	31.6 - 32.3	914
3	38.8	0.93 - 1.46	29.3 - 30.0	918
4	25.3	2.00 - 2.49	27.5 - 28.3	920
5	20.7	2.52 - 3.19	25.7 - 26.5	930

a 0.1 value difference in γ between CH_4-air and oxy-CH_4 combustion. The decrease in in-cylinder temperature and pressure during ignition and combustion can be attributed to a reduction of S_L as shown in Table 7. CO_2 (1.795 g/m^3 [53]) has a higher density than N_2 (0.808 g/m^3 [54]), which means the in-cylinder mixture is denser, thereby hindering flame propagation and resulting in a slower combustion process. Additionally, these reductions in temperature and pressure can be linked to the lower thermal diffusivity of CO_2 (0.111 cm^2/s at standard conditions) when compared to N_2 (0.222 cm^2/s at standard conditions) due to the fact that CO_2 represents a higher thermal mass than N_2 with a reduced thermal conductivity. With the increased replacement of N_2 by CO_2, CoV_{IMEP} increases by 2%.

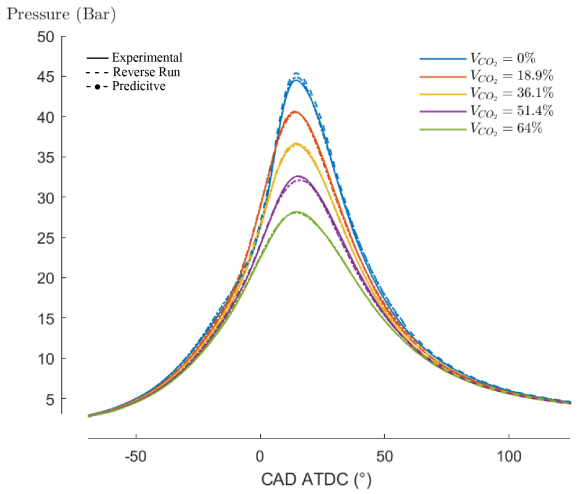

Figure 5. Measured, reverse run and predicted In-cylinder pressures

This is due to 1) higher variations in gas compositions and residual gas within the cylinder at the time of ignition, especially near the spark plug [38] and 2) the increased combustion duration, which is explained in the following section. As the burning rate increases, the variations in the flame development process and the subsequent combustion process decreases [38, 55]. It is interesting to note that due to the oxygen-enrichment of the cylinder contents in comparison to air as more CO_2 is introduced to the fuel-oxidizer mixture (i.e. considering the fourth column of Table 4), the dilution limit of methane combustion is extended from conventional air-lean operation. However, due to the high overall concentration of diluent in the chamber and the use of CO_2 in place of N_2, there is no thermal efficiency benefit due to decreased γ, as previously indicated, and increased combustion duration.

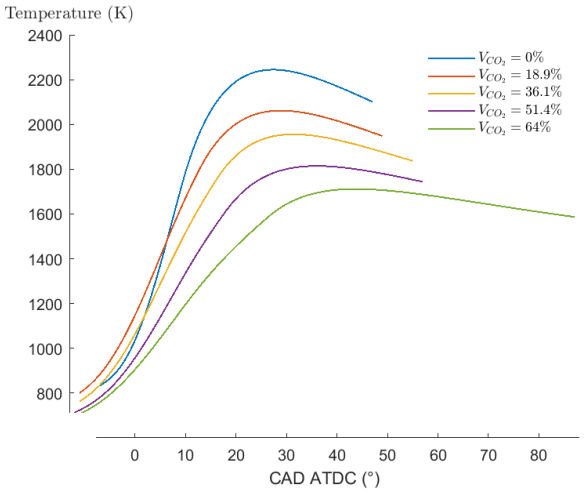

Figure 6. In-cylinder temperatures in function of CAD ATDC

Impact of oxidizer composition on heat release rate and combustion phasing

Starting from methane-air combustion to the complete replacement of N_2 by CO_2, the peak heat release rate is approximately halved as seen in Figure 8, which is due primarily to the increased heat retention capacity of

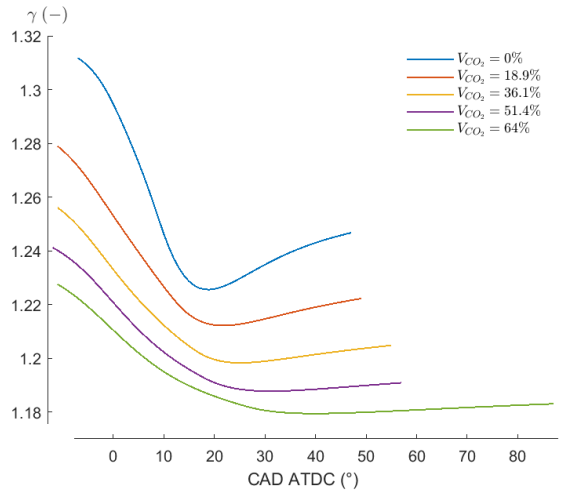

Figure 7. In-cylinder γ in function of CAD ATDC

CO_2. It should be noted that the duration of heat release lasts longer for higher volumes of CO_2, which can be further explained through combustion phasing. Figure 9 also shows the variation in IT and the combustion phasing where respectively 2%, 10%, 50% and 90% of the fuel is burned (CA2, CA10, CA50 and CA90) with increasing CO_2 composition. It is evident from Figure 9 that the value of

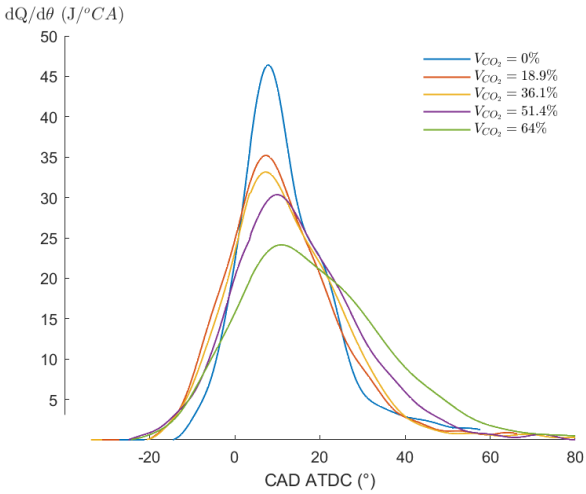

Figure 8. $dQ/d\theta$ in function of CAD ATDC

IT has to be advanced up to 16 CAD from the baseline methane-air case when all the N_2 is replaced with CO_2 in order to maintain MBT timing. Figure 10 shows that even with the advancement of IT, there is an increase in combustion duration by 23 CAD in values of CA10 to CA90 for full CO_2 dilution. Therefore the heat release event occurs over a longer time with the increase in CO_2 dilution. These trends confirm the previously mentioned effect of CO_2 on combustion speed. In the initial flame development phase (i.e. IT-CA2) there is also an observable increase due to its strong dependency on laminar flame speed [38]. It is noted that these combustion retarding effects due to the presence of increased CO_2 appear to dominate any reactivity promoting effects of the oxygen-enriched environments in the tested conditions, as the trends related to the length of the combustion event are all monotonically increasing with higher CO_2 concentration.

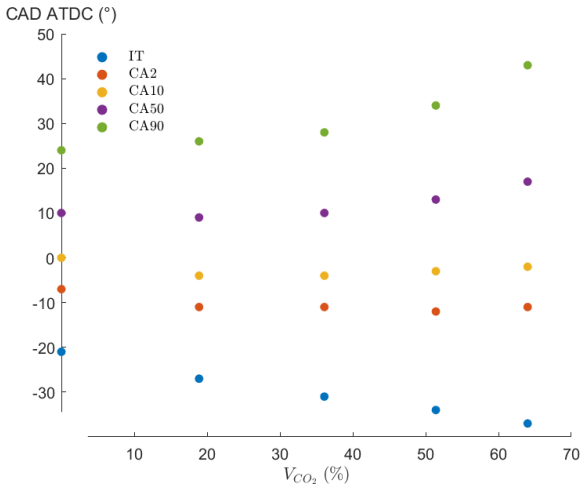

Figure 9. IT, CA2, CA10, CA50 and CA90 for changing oxidizer compositions

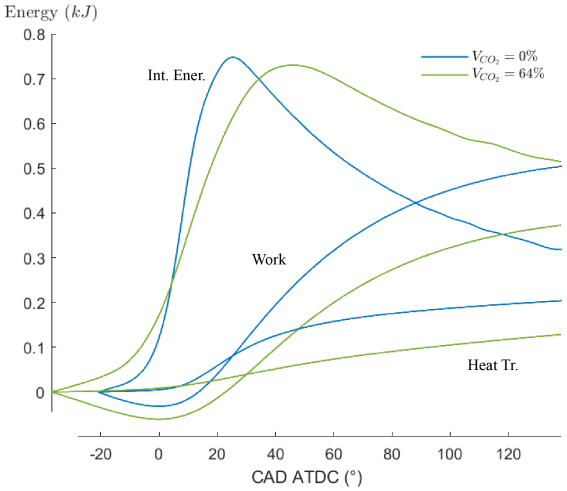

Figure 11. Cumulative Work, internal energy and heat losses in function of CAD ATDC

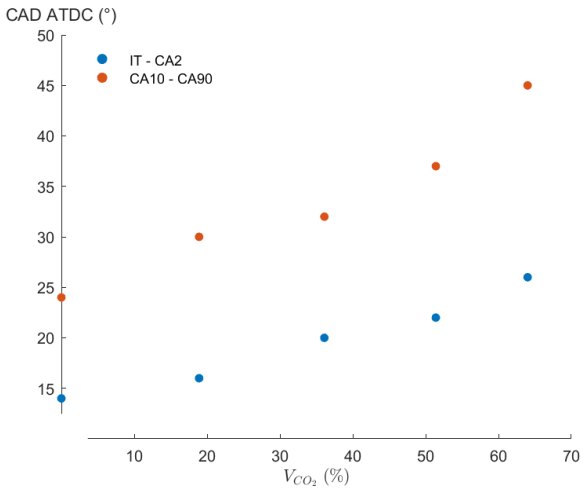

Figure 10. flame development phase and combustion duration for changing oxidizer compositions

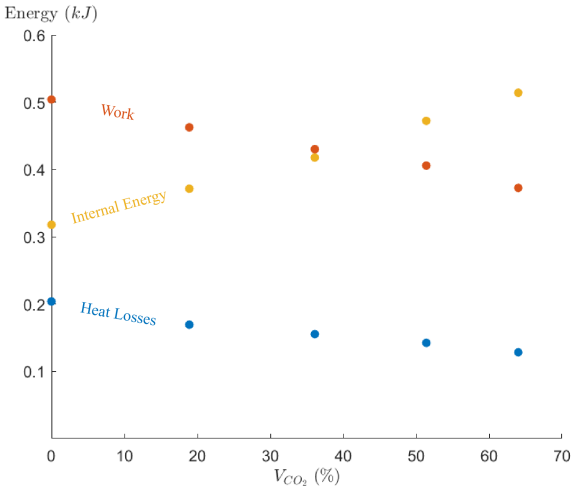

Figure 12. cumulative Work, internal energy and heat losses at EVO

Oxy-methane engine efficiency under CO_2 dilution

The value of indicated efficiency (η_i) is shown in Table 7 and it is evident that with full CO_2 dilution, η_i reduces by 10%, indicating that significant CO_2 dilution in the oxy-CH_4 combustion mode reduces the fraction of work produced from the injected chemical energy of the fuel. This can be further explained by analyzing the energy balance. Equation 8, which determines the apparent rate of heat release, can be split up into 3 parts consisting of work, internal energy and heat losses. Figures 11 and 12 show the cumulative work, internal energy and heat losses for CH_4-air and oxy-CH_4 combustion. The decrease in heat losses for oxy-CH_4 combustion can be logically explained by the decrease in temperature in the combustion chamber, leading to lower temperature gradients between the hot gas and walls, and therefore reduced wall heat loss (Figures 11 and 12). The shift in internal energy and work when comparing CH_4-air and oxy-CH_4 combustion can be explained through two mechanisms. The first is the impact of γ of the mixture, summarized succinctly by the equation for ideal efficiency in Equation 7. While this equation is only valid for the ideal thermodynamic cycle, the general trend of increasing thermal efficiency with increasing γ is also true of real-world IC engines. When considering two operating conditions where the CO_2 in the oxidizer stream is increased, the same heat is released by combusting the fuel in both cases, but due to the thermal quenching effect of increased CO_2, there is a reduction in temperature and pressure in the combustion chamber. This results in less mechanical work produced by the heat release from methane and a higher enthalpy of the exhaust gasses. The second mechanism governing the shift between internal energy and work is through the increase of combustion duration as CO_2 dilution increases. When the oxidizer mixture contains more CO_2 and becomes increasingly lean with the respect to oxygen, the duration of the combustion event increases and the degree of constant volume combustion, η_{dcv} in Equation 5, reduces by 8% due to the reduction in combustion speed. This renders the process less isochoric and results in relatively more fuel chemical energy used to raise the internal energy of the products of combustion in comparison to useful work output. The exhaust temperatures given in Table 7 show an increasing trend which supports these findings. Additionally, The cumulative heat release should equal the total energy content of the injected fuel during the cycle. However, this is only true in the ideal case where the amount of unburned fuel is zero. In this study, the unburned fuel content in the exhaust was not

directly measured, and the wall temperature was estimated from a temperature probe located near the cylinder wall. Even though the individual contributions of these losses are uncertain, their combined effect should equal the difference between the total fuel energy and the sum of the work and the internal energy contributions. This is represented as 'Losses' in Table 8. To conclude, even though there is a reduction of losses for oxy-CH_4 with CO_2 dilution, there is also a decrease in combustion performance explained by both mechanisms. This suggests that the use of CO_2-diluted oxy-methane combustion is most suitable in a combined heat and power (CHP) application. The valorization of the increased enthalpy in the high-temperature exhaust gasses could offset the decrease in mechanical work when shifting from conventional methane-air to CO_2-diluted oxy-methane combustion with the additional benefit of avoiding NO_x emissions.

Table 8. Work, internal energy and loss as percentages of the overall injected chemical energy for both operating condition in Figure 11.

	Work (%)	Internal energy (%)	Losses (%)
$Air - CH_4$	34.4	40.3	25.3
$Oxy - CH_4$	26.1	54.5	19.4

Prediction of generalized instability limit for a range of oxidizer mixtures using premixed turbulent combustion theory

While the previous section offered a view of the combustion performance of oxy-methane diluted with CO_2, there remains the possibility to provide insight into the dilution limit possible in oxy-methane reciprocating engines. Implementing the zero-NO_x, oxy-fuel CHP units mentioned earlier will require a thorough understanding of the limits of operability of such an engine platform, and it is the goal of this section to offer a generalized characterization of this operating limit based on the fundamental theory of turbulent combustion. While the test bench is suitable for proof-of-concept studies, it operates with a relatively low compression ratio and is naturally aspirated. This configuration deviates from modern stationary gas engines, which are typically turbocharged and highly efficient. A key focus of this work is to examine how CO_2-diluted oxy-CH_4 combustion differs fundamentally from conventional air-CH_4 combustion. The aim is to derive findings that are broadly applicable to all spark ignited reciprocating engines. From the predictive model of GT-Power, the effect of CO_2 dilution on the laminar and turbulent flame speed as a function of CAD is shown in Figure 13. The combustion loci along with 5 specific Mass Fraction Burned (MFB) values, namely, CA2, CA10, CA50, CA90 and EOC (CA99) are visualised. As N_2 is replaced by CO_2, the laminar and turbulent flame speeds decrease as expected. Note that this decline in S_L occurs at a decreasing rate for increased CO_2 dilution, because there is the competing effect of increasing O_2 concentration in the chamber from the first ($V_{O_2} = 19\%$) to the last experimental condition ($V_{O_2} = 32.6\%$). The increasing oxygen-enrichment of the chamber partially offsets the decrease in S_L caused by the overall increased

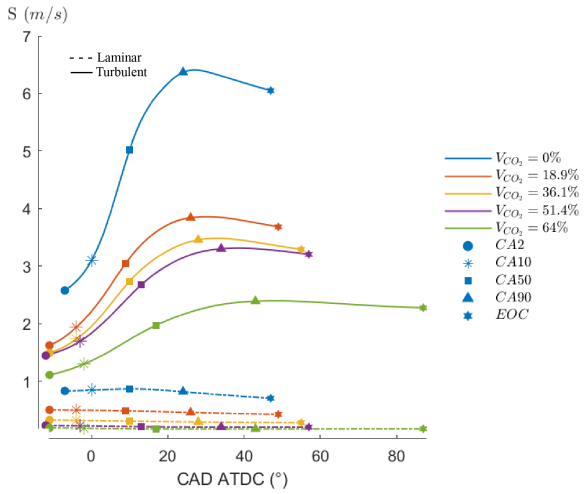

Figure 13. S_L and S_T in function of CAD ATDC

dilution and higher concentrations of CO_2. This is evidenced by the slightly increased S_L for very lean CO_2 diluted oxy-methane as opposed to air-methane mixtures in Figure 2, which serves to extend the air-lean instability limit. The impact of CO_2 dilution in oxy-fuel combustion is further highlighted in the combustion regime diagram of Figure 14, which illustrates three combustion modes plotted on axes of the Damköhler number (Da) versus the turbulent Reynolds number (Re_T). The combustion loci at CA90 are visualized, here S_T/S_L is at its maximum, which follows the methodology used in [56]. The regimes are categorized as follows: weak turbulence, where $u_k^t/S_L < 10^{-2}$, reaction sheets, where the Kolmogorov microscale (l_k) is greater than the flame thickness (δ_L) and distributed reactions, where the turbulent length scale (L_T) is smaller than δ_L [56]. Most of the data points lie below the $l_k = \delta_L$ line, and as nitrogen (N_2) is replaced by carbon dioxide (CO_2), these points move further away from the line. This highlights the critical role of laminar flame speed in determining the combustion regime in oxy-fuel engines. As the CO_2 concentration increases in the

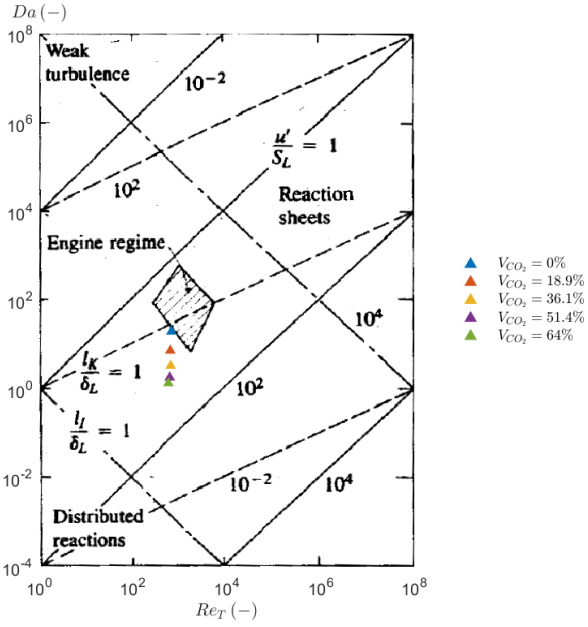

Figure 14. The combustion regimes as a function of Da and Re_T proposed by Heywood [38]

oxidizer mixture and λ' increases, the laminar flame speed decreases, increasing the chemical timescale (δ_L/S_L) and reducing Da. This effect causes the operation of the CO_2-diluted oxy-methane engine to deviate significantly from the typical regime found in conventional engines as demarcated in Figure 14 (the shaded region labeled 'Engine regime'). Figure 15 illustrates the combustion regimes proposed by

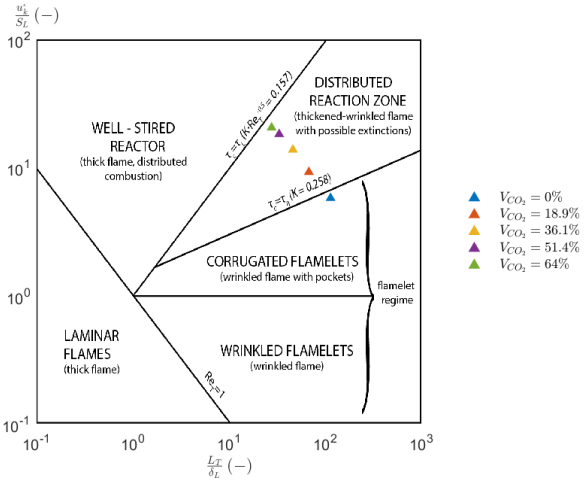

Figure 15. The combustion regimes proposed by Borghi. [45, 35]

Borghi [45], expressed in terms of u_k^t/S_L and L_T/δ_L, along with the flow timescale ($\tau_{flow} = \tau_L$), Kolmogorov timescale (τ_η) and chemical timescale ($\tau_{chemical} = \tau_c$). The combustion loci at CA90 are visualized, where S_T/S_L is at its maximum. It should be stated that this diagram does not consider the influence of the Lewis number (Le), which is approximately unity for methane-air combustion near stoichiometry. In Figure 15, stoichiometric CH_4-air combustion falls within the regime of corrugated flamelets, which are characterized by a flame thickness that is smaller than the Kolmogorov length scale ($\delta_L < \eta$), and are therefore not perturbed by turbulent fluctuations. However, as nitrogen (N_2) is replaced by carbon dioxide (CO_2), the operation shifts further away from this regime into the thickened-wrinkled flame regime, where η becomes less than the flame thickness, suggesting the smallest turbulent eddies can disturb the flame structure and cause possible extinctions. This further underscores the critical role of laminar flame

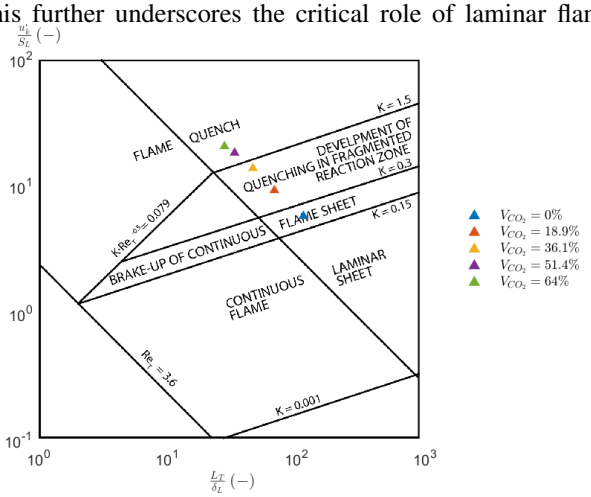

Figure 16. The Borghi diagram proposed by Bradley et al.[35]

speed in oxy-fuel combustion engines. The decrease in laminar flame speed due to the presence of CO_2 causes the combustion locus to shift upward and to the left, as the flame thickness (δ_L) is inversely proportional to the laminar flame speed. Continuing with the concept of flame extinction at the instability limit, Figure 16 illustrates the combustion regimes proposed by Bradley et al. [35], expressed in terms of u_k^t/S_L and L_T/δ_L. The combustion loci at CA90 are visualized, where S_T/S_L is at its maximum. Stoichiometric CH_4-air combustion falls within the regime of continuous laminar flame sheets at ignition and early mass fraction burned (MFB) loci, gradually moving toward potential flame break-up. However, with increasing dilution by carbon dioxide (CO_2), the points shift further away from this regime into the development of quenching in fragmented reaction zones. Under operating conditions with 51.4% and 64% CO_2 in the oxidizer mixture, the points move distinctly into the quenching region, where bulk extinguishing events are expected. This shift helps explain the experimentally observed combustion instability, as measured by CoV_{IMEP}. Similar to Figure 15, the reduction in laminar flame speed causes the combustion locus to shift upward and to the left.The effect of CO_2 dilution on flame quenching is also shown in Figure 17. The ratio of the turbulent burning

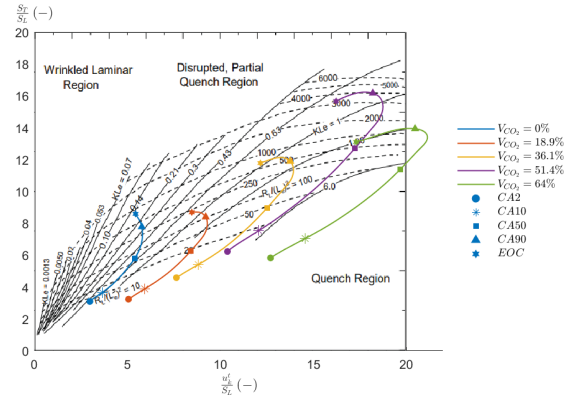

Figure 17. Combustion locus on the Bradley diagram [36] with CA2, CA10, CA50, CA90 and EOC

velocity to laminar flame speed is plotted against the ratio of the turbulence intensity to laminar flame speed in the Bradley diagram and the solid curves represent increasing values of the product of K and Le from left to right. The physical interpretation is that larger K suggests that the relatively long chemical to eddy lifetime can result in excessive flame stretch and partial quenching and $Le > 1$ implies that the flame is diffusing its heat more rapidly than fresh mixture diffuses to the flame for it to propagate (where stoichiometric combustion processes of hydrocarbon fuels have $Le \approx 1$ and air-lean operation is $Le > 1$). As the product of these two quantities increases, it is generally expected that bulk flame quenching during the formation of the flame kernel becomes more likely and combustion instability is encountered. The combustion loci along with 5 specific MFB values, namely, CA2, CA10, CA50, CA90 and EOC (CA99) are superimposed on the Bradley diagram consisting of contours of constant $K\,Le$. As N_2 is replaced by carbon dioxide CO_2, the decreasing laminar flame speed causes the combustion locus to shift upward and to the right, accompanied by

higher values of $K\,Le$ during the early stages of combustion and flame development. Under the most extreme operating conditions, the combustion speed is significantly reduced, pushing the combustion locus into the quenching region. From Equation 20, the values of $K\,Le$ are calculated for the combustion loci and five specific MFB points, CA2, CA10, CA50, CA90, and EOC (CA99), and then plotted against CAD ATDC in Figure 18. The combustion loci

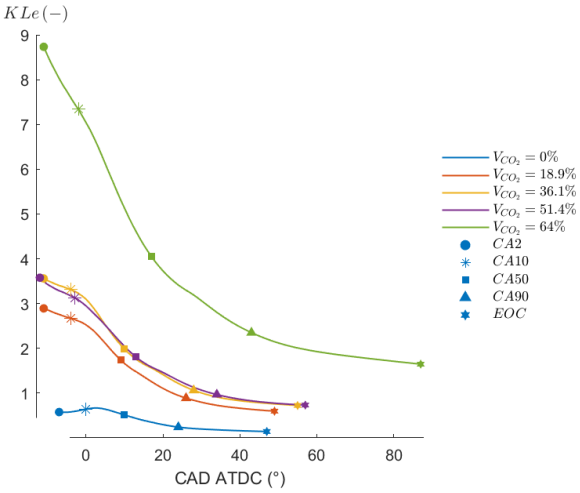

Figure 18. $K\,Le$ in function of CAD ATDC calculated from the bradley diagram

shift toward higher $K\,Le$ values under operating conditions with increased CO_2 dilution. It is important to note, as Bradley et al. [36] indicated, that the calculated $K\,Le$ values using the correlation of Equation 20 are only accurate for values below 0.63, which may explain why the $K\,Le$ values for all conditions except CH_4-air combustion are likely overestimated. In Figure 19, the $K\,Le$ values are evaluated directly using Equation 17 and multiplied by the computed Le using Equation 18. In Table 9 the calculated Lewis

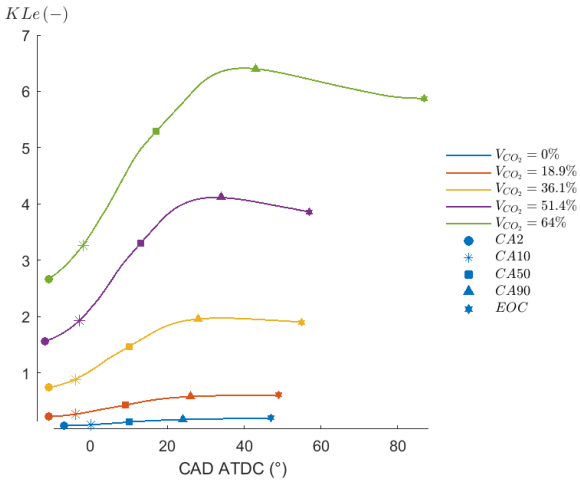

Figure 19. $K\,Le$ in function of CAD ATDC calculated from Equation 17

Table 9. Le at different MFB for every operating condition.

Sl. No.	Le (CA2)	Le (CA10)	Le (CA50)	Le (CA90)
1	0.964	0.951	0.935	0.931
2	0.913	0.904	0.891	0.888
3	0.874	0.868	0.857	0.854
4	0.843	0.840	0.831	0.829
5	0.819	0.817	0.812	0.811

numbers are displayed for the different MFB points. It is clear that the Lewis numbers remains relatively constant during the combustion process. For calculating the $K\,Le$ values, a constant Le at CA2 is used. Compared to the derived $K\,Le$ values from the Bradley diagram in Figure 18, the overall shape of the curves differs significantly, with a notable rising trend instead of the expected falling trend. This upward trend can be attributed to u_k^t/S_L, which shows a steep increase from the start of combustion, as indicated by Equation 17. Therefore, it can be concluded that directly evaluating K from Equation 17 and plotting it on the Bradley diagram is not generally a valid approach for spark ignition (SI) engines. The Bradley diagram is constructed empirically from experiments involving explosions in fan-stirred bombs and burners [41, 42, 43, 44, 57], which assumes isotropic turbulence, a condition not present in the combustion chamber of the engine used in this research, and not typically expected in reciprocating engines. It is worthwhile to note that the Le behavior for combustion heavily diluted by CO_2 is significantly different to that of air dilution. For air-lean operation, Le tends to rise above unity as the concentration of oxygen and nitrogen is increased. $CO2$, on the other hand, has a low thermal diffusivity that is comparable to methane and also has a relatively high mass diffusivity with methane, both of which lead to sub-unity Le in the case of oxy-methane combustion with CO_2-dilution. Because Le decreases with increasing CO_2 dilution rates, this suggests that any quenching prediction captured by larger values $K\,Le$ is dominated by increasing values of K, and is therefore tied to the impact of increasing dilution on reducing S_L as shown in Figure 13 (and therefore increasing the chemical time scale in Equation 15). Now the theoretically

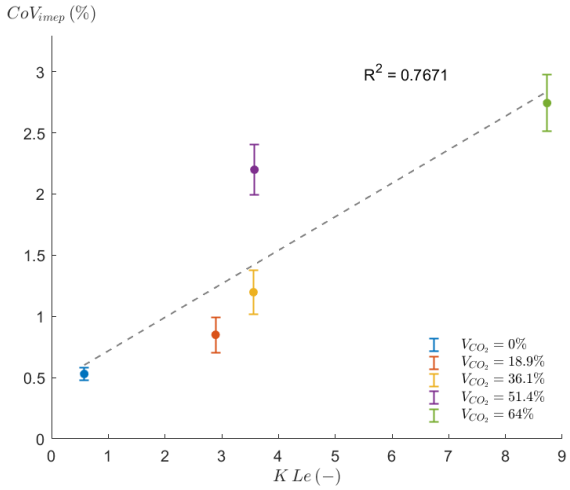

Figure 20. CoV_{imep} in function of $K\,Le$ calculated from the Bradley diagram

predicted $K\,Le$ values, which indicate a proclivity for bulk flame quenching, are compared to experimentally measured combustion instability using the coefficient of variation of indicated mean effective pressure (CoV_{IMEP}). The calculated $K\,Le$ values from the Bradley diagram (i.e. Equation 20) and from Equation 17 are shown in Figure 20 and Figure 21, respectively, plotted against CoV_{IMEP} for the same operating conditions and at CA2. Two dotted trendlines represent each operating condition along with

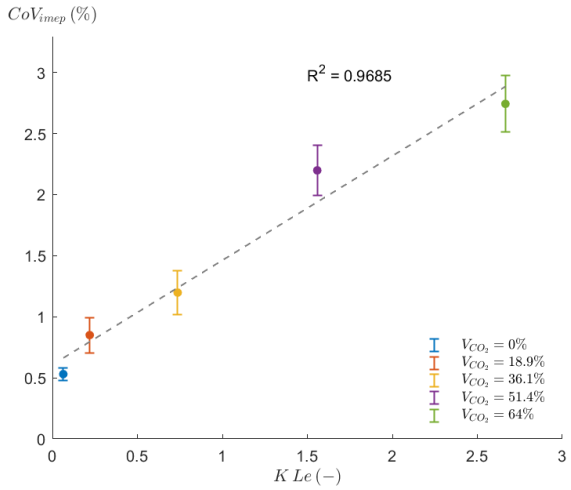

Figure 21. CoV_{imep} in function of $K\,Le$ calculated from Equation 17

their corresponding R^2 values. Based on these R^2 values, it is evident that the $K\,Le$ values evaluated directly from Equation 17 are more strongly correlated with CoV_{IMEP} (i.e. experimentally measured instability) than are those derived from the Bradley diagram. The improved accuracy is primarily because the $K\,Le$ values obtained using the correlation in Equation 20 are only reliable below 0.63 and, as mentioned, the expression is built on the assumption of isotropic turbulence, which is not expected in reciprocating engines. Therefore, a direct evaluation of K from theory appears to be more appropriate for the prediction of the dilution limit in reciprocating engines. The $K\,Le$ predictions are particularly significant at lower MFB locations, as the flame is more prone to quenching during the initial stages of combustion [38, 58]. The high correlation strength present in Figure 21 suggests that premixed turbulent combustion theory effectively captures the instability limits across a wide range of oxidizer mixtures, including air-lean conditions and oxygen-enriched operation where nitrogen is replaced by CO_2.

Conclusions

This study undertook a numerical and experimental investigation of CO_2 diluted oxy-CH_4 combustion in a reciprocating engine. oxidizer composition was gradually changed from stoichiometric air-CH_4 combustion towards CO_2 diluted oxy-CH_4 combustion with an excess of O_2. Experiments confirmed that the overall in-cylinder pressure and temperature decreased with increased CO_2 dilution due to the reduction in combustion speed and γ. The higher density of CO_2 and the lower thermal diffusivity of CO_2 compared to N_2 acted to hinder flame propagation with increased CO_2 replacement resulting in a slower combustion process. The heat release rate occurred over a larger range of CAD and the peak heat release rate decreases. In addition, the CoV_{IMEP} increases as the engine approaches the dilution limit. The energy balance indicated that while there is a loss of efficiency and useful work produced by the engine, the heat losses to the wall are actually decreased as a relatively larger share of the chemical energy in fuel is transferred to the exhaust gasses. This suggested that a combined heat and power application is likely the most practical option for a methane CO_2-diluted oxy-methane reciprocating engine, as the losses of fuel conversion efficiency can be offset by the valorization of additional energy in the exhaust.

A further exploration of the instability limit of oxy-methane reciprocating engines was undertaken using a predictive model of combustion to determine the relevant non-dimensional quantities to describe the lean limit of premixed, turbulent flames. While such theory was originally developed to describe the air-lean limit of premixed flame propagation, this was extended to describe the dilution limit for generalised oxidizer blends consisting of O_2, N_2 and CO_2. The results showed that the quantity $K\,Le$ increased as the oxidizer shifted to the CO_2 diluted oxy-fuel mode, moving the combustion process towards the quench region. This phenomenon was dominated by a rising K when adding CO_2, as the Le of the in-cylinder mixture decreases with increased CO_2 dilution because of the decreased thermal diffusivity compared to N_2. Further, a correlation between CoV_{IMEP} and $K\,Le$ indicated that a previously developed expression for K was not generally appropriate in reciprocating engines due to assumptions of isotropic turbulence. Rather, a direct evaluation of K was preferred, as indicated by the increased strength of the correlation between calculated $K\,Le$, a theoretical prediction of flame quenching, and CoV_{IMEP}, an experimental measurement of combustion instability.

From the correlation, it was observed that lower values of $K\,Le$ are associated with reduced CoV_{IMEP}. As a next step, H_2 will be investigated in the CO_2-diluted oxy-fuel mode, as the addition of hydrogen is expected to increase the laminar flame speed and thus promote more stable flame propagation. Since K is proportional to $1/S_L^2$, a higher flame speed directly contributes to improved combustion stability. Furthermore, the inherently low Le of hydrogen is also expected to enhance stability by mitigating diffusive-thermal instabilities. Therefore, the dilution limits of such flames will be systematically explored.

Declaration of conflicting interests

The authors declare that there is no conflict of interest.

References

[1] for Communication DG. A european green deal striving to be the first climate-neutral continent, 2022. URL https://commission.europa.eu/strategy-and-policy/priorities-2019-2024/european-green-deal_en.

[2] Yue Z, Wang X, Liu H et al. Exploring the application of oxy-fuel combustion to methanol spark ignition engines. *Applied Energy* 2024; 367: 123449.

[3] Senecal K and Leach F. *Racing toward zero: the untold story of driving green*. SAE International, 2021.

[4] Talei S, Fozer D, Varbanov PS et al. Oxyfuel combustion makes carbon capture more efficient. *ACS omega* 2024; 9(3): 3250–3261.

[5] Li X, Peng Z, Pei Y et al. Oxy-fuel combustion for carbon capture and storage in internal combustion engines–a review. *International Journal of Energy Research* 2022; 46(2): 505–522.

[6] Ferrari J. *Renewable fuels for long-term energy storage*. Elsevier, 2021. pp. 109–138. DOI:10.1016/b978-0-12-819873-5.00004-6.

[7] Dias V, Pochet M, Contino F et al. Energy and economic costs of chemical storage. *Frontiers in mechanical engineering* 2020; 6: 21.

[8] Rixhon X, Limpens G, Jeanmart H et al. Taxonomy of the fuels in a whole-energy system. *Frontiers in Energy Research* 2021; 9: 660073.

[9] Ditaranto M and Hals J. Combustion instabilities in sudden expansion oxy–fuel flames. *Combustion and flame* 2006; 146(3): 493–512.

[10] Serrano J, Martín J, Gómez-Soriano J et al. Theoretical and experimental evaluation of the spark-ignition premixed oxy-fuel combustion concept for future co2 captive powerplants. *Energy conversion and Management* 2021; 244: 114498.

[11] Van Blarigan A, Seiser R, Chen J et al. Working fluid composition effects on methane oxycombustion in an si-engine: Egr vs. co2. *Proceedings of the Combustion Institute* 2013; 34(2): 2951–2958.

[12] de Boer PCT and Hulet JF. Performance of a hydrogen-oxygen-noble gas engine. *International Journal of Hydrogen Energy* 1980; 5(4): 439–452.

[13] Killingsworth NJ, Rapp VH, Flowers DL et al. Increased efficiency in si engine with air replaced by oxygen in argon mixture. *Proceedings of the Combustion Institute* 2011; 33(2): 3141–3149.

[14] Kang Z, Wu Z, Zhang Z et al. Study of the combustion characteristics of a hcci engine coupled with oxy-fuel combustion mode. *SAE International Journal of Engines* 2017; 10(3): 908–916.

[15] Kang Z, Chen S, Wu Z et al. Simulation study of water injection strategy in improving cycle efficiency based on a novel compression ignition oxy-fuel combustion engine. *SAE International Journal of Engines* 2018; 11(6): 935–946.

[16] Kuroki R, Kato A, Kamiyama E et al. Study of high efficiency zero-emission argon circulated hydrogen engine. Technical report, SAE Technical Paper, 2010.

[17] Killingsworth NJ, Rapp VH, Flowers DL et al. Increased efficiency in si engine with air replaced by oxygen in argon mixture. *Proceedings of the Combustion Institute* 2011; 33(2): 3141–3149.

[18] Van Blarigan A, Kozarac D, Seiser R et al. Experimental study of methane fuel oxycombustion in a spark-ignited engine. *Journal of Energy Resources Technology* 2014; 136(1): 012203.

[19] Van Blarigan A, Kozarac D, Seiser R et al. Spark-ignited engine nox emissions in a low-nitrogen oxycombustion environment. *Applied energy* 2014; 118: 22–31.

[20] Nemitallah MA, Habib MA, Badr HM et al. Oxy-fuel combustion technology: current status, applications, and trends. *International Journal of Energy Research* 2017; 41(12): 1670–1708.

[21] Baughn J and Bagheri N. The effect of thermal matching on the thermodynamic performance of gas turbine and ic engine cogeneration systems 1987; .

[22] Abbasi M, Chahartaghi M and Hashemian SM. Energy, exergy, and economic evaluations of a cchp system by using the internal combustion engines and gas turbine as prime movers. *Energy conversion and management* 2018; 173: 359–374.

[23] Kanoglu M, Işık SK and Abuşog˘lu A. Performance characteristics of a diesel engine power plant. *Energy Conversion and Management* 2005; 46(11-12): 1692–1702.

[24] Seo SB, Kim HW, Kang SY et al. Techno-economic comparison between air-fired and oxy-fuel circulating fluidized bed power plants with ultra-supercritical cycle. *Energy* 2021; 233: 121217.

[25] Abraham B, Asbury J, Lynch E et al. Coal-oxygen process provides co/sub 2/for enhanced recovery. *Oil Gas J;(United States)* 1982; 80(11).

[26] Shaw R and Oman H. Non-air working fluids for closed-cycle diesel engines. In *Proc., Intersoc. Energy Convers. Eng. Conf.;(United States)*, volume 2. The Boeing Company, Seattle, Washington.

[27] Zheng M, Reader G, Potter I et al. A thermodynamic model of an air-independent idi diesel engine system. Technical report, SAE Technical Paper, 1992.

[28] Hawley J, Ashcroft S and Patrick M. The design, construction and testing of a non air-breathing diesel engine research facility for autonomous underwater

vehicle applications. Technical report, SAE Technical Paper, 1992.

[29] Hawley J, Reader G, Zheng M et al. Investigations on carbon dioxide/oxygen breathing diesel engines—results from an international collaborative project. *Underwater Technology* 1998; 23(3): 109–121.

[30] Hawley J and Reader GT. Experimental performance results from a carbon dioxide/oxygen breathing diesel engine. *SAE transactions* 1994; : 1757–1761.

[31] Wu HW, Wang RH, Chen YC et al. Influence of port-inducted ethanol or gasoline on combustion and emission of a closed cycle diesel engine. *Energy* 2014; 64: 259–267.

[32] Wu ZJ, Yu X, Fu LZ et al. A high efficiency oxyfuel internal combustion engine cycle with water direct injection for waste heat recovery. *Energy* 2014; 70: 110–120.

[33] Yu X and Wu ZJ. Simulation on effect of egr on oxy-fuel ic engine. *Applied Mechanics and Materials* 2012; 130: 790–795.

[34] Yu X, Wu Z, Fu L et al. Study of combustion characteristics of a quasi internal combustion rankine cycle engine. Technical report, SAE Technical Paper, 2013.

[35] Abdel-Gayed R, Bradley D and Lung FK. Combustion regimes and the straining of turbulent premixed flames. *Combustion and Flame* 1989; 76(2): 213–218.

[36] Bradley D, Lau A, Lawes M et al. Flame stretch rate as a determinant of turbulent burning velocity. *Philosophical Transactions of the Royal Society of London Series A: Physical and Engineering Sciences* 1992; 338(1650): 359–387.

[37] Pochet M, Jeanmart H and Contino F. Uncertainty quantification from raw measurements to post-processed data: A general methodology and its application to a homogeneous-charge compression–ignition engine. *International Journal of Engine Research* 2020; 21(9): 1709–1737.

[38] Heywood JB. *Internal combustion engine fundamentals*. McGraw-Hill Education, 2018.

[39] Shudo T and Nabetani S. Analysis of degree of constant volume and cooling loss in a hydrogen fuelled si engine. Technical report, SAE Technical Paper, 2001.

[40] NASA-TM-4513. Coefficients for calculating thermodynamic and transport properties of individual species. `https://ntrs.nasa.gov/citations/19940013151`, 1993.

[41] Abdel-Gayed R, Bradley D and Lawes M. Turbulent burning velocities: a general correlation in terms of straining rates. *Proceedings of the Royal Society of London A Mathematical and Physical Sciences* 1987; 414(1847): 389–413.

[42] Abdel-Gayed R, Al-Khishali K and Bradley D. Turbulent burning velocities and flame straining in explosions. *Proceedings of the Royal Society of London A Mathematical and Physical Sciences* 1984; 391(1801): 393–414.

[43] Abdel-Gayed R, Bradley D, Hamid M et al. Lewis number effects on turbulent burning velocity. In *Symposium (international) on combustion*, volume 20. Elsevier, pp. 505–512.

[44] Abdel-Gayed R and Bradley D. Criteria for turbulent propagation limits of premixed flames. *Combustion and Flame* 1985; 62(1): 61–68.

[45] Borghi R. On the structure and morphology of turbulent premixed flames. In *Recent advances in the aerospace sciences: In honor of luigi crocco on his seventy-fifth birthday*. Springer, 1985. pp. 117–138.

[46] Peters N. Laminar flamelet concepts in turbulent combustion. In *Symposium (International) on combustion*, volume 21. Elsevier, pp. 1231–1250.

[47] Zhou CW, Li Y, Burke U et al. An experimental and chemical kinetic modeling study of 1, 3-butadiene combustion: Ignition delay time and laminar flame speed measurements. *Combustion and Flame* 2018; 197: 423–438.

[48] Hu E, Li X, Meng X et al. Laminar flame speeds and ignition delay times of methane–air mixtures at elevated temperatures and pressures. *Fuel* 2015; 158: 1–10.

[49] Hu X, Yu Q, Liu J et al. Investigation of laminar flame speeds of ch4/o2/co2 mixtures at ordinary pressure and kinetic simulation. *Energy* 2014; 70: 626–634.

[50] Kar T, Zhou Z, Brear M et al. A comparative study of directly injected, spark ignition engine combustion and energy transfer with natural gas, gasoline, and charge dilution. *SAE International Journal of Fuels and Lubricants* 2022; 15(04-15-02-0009): 199–220.

[51] Fraioli V, Di Maio D, Napolitano P et al. A joint work to develop a predictive 1d modelling approach for heavy duty gaseous fueled engines through experiments and 3d cfd simulations. Technical report, SAE Technical Paper, 2023.

[52] d'Antuono G, Galloni E, Lanni D et al. Assessment of combustion development and pollutant emissions of a spark ignition engine fueled by ammonia and ammonia-hydrogen blends. *International Journal of Hydrogen Energy* 2024; 85: 191–199.

[53] Engineeringtoolboxcom. Carbon Dioxide - Thermophysical Properties. `https://www.engineeringtoolbox.com/CO2-carbon-dioxide-properties-d_2017.html`, 2023.

[54] Engineeringtoolboxcom. Nitrogen - Thermophysical Properties. `https://www.`

engineeringtoolbox.com/nitrogen-d_1421.html, 2023.

[55] Maurya RK, Maurya L and Luby. *Reciprocating engine combustion diagnostics*. Springer, 2019.

[56] Abbasi Atibeh P, Brear MJ, Dennis PA et al. Lean limit combustion analysis for a spark ignition natural gas internal combustion engine. *Combustion science and technology* 2013; 185(8): 1151–1168.

[57] Abdel-Gayed RG and Bradley D. A two-eddy theory of premixed turbulent flame propagation. *Philosophical transactions of the royal society of London Series A, Mathematical and physical sciences* 1981; 301(1457): 1–25.

[58] Gillespie L, Lawes M, Sheppard C et al. Aspects of laminar and turbulent burning velocity relevant to si engines. *SAE transactions* 2000; : 13–33.